Journal of Materials Chemistry A

# Mechanistic Insights into Metal, Nitrogen Doped Carbon Catalysts for Oxygen Reduction: Progress in Computational Modeling

| | |
|---|---|
| Journal: | *Journal of Materials Chemistry A* |
| Manuscript ID | TA-REV-07-2022-005991.R1 |
| Article Type: | Review Article |
| Date Submitted by the Author: | 14-Oct-2022 |
| Complete List of Authors: | Li, Boyang ; Univeristy of Pittsburgh, Mechanical Engineering and Materials Science<br>Holby, Edward; Los Alamos National Laboratory, Sigma Division<br>Wang, Guofeng; University of Pittsburgh, Mechanical Engineering and Materials Science |
| | |

# Mechanistic Insights into Metal, Nitrogen Doped Carbon Catalysts for Oxygen Reduction: Progress in Computational Modeling

Boyang Li, [1] Edward F. Holby, [2] and Guofeng Wang [1]

[1] *Department of Mechanical Engineering & Materials Science, University of Pittsburgh, Pittsburgh, PA, 15261, USA*

[2] *Sigma Division, Los Alamos National Laboratory, Los Alamos, NM 87545, USA*

**Abstract:**

Metal and nitrogen doped carbon materials (denoted as M-N-C) synthesized through high-temperature pyrolysis have been found to exhibit activity for oxygen reduction reaction (ORR) approaching that of Pt and electrochemical stability higher than previous $MN_4$-containing macrocyclic molecular catalysts. Tremendous efforts have thus been devoted to the advancement of M-N-C catalysts as an economical alternative to Pt-based catalysts for proton exchange membrane fuel cell cathodes with a focus on simultaneously improving activity and stability. To this end, novel computational modeling techniques have been developed and applied to acquire knowledge crucial for accelerating the pace of M-N-C catalyst development. In this review, recent progress in computational method development, as well as the predictions of chemical structure of active sites, reaction pathways, ORR kinetics, and catalyst stability in electrochemical environments, are critically surveyed. Moreover, the crucial role of computational modeling to elucidate the functional mechanism of M-N-C catalysts for ORR in acid media and enable rational design of M-N-C catalysts is discussed with a visionary outlook for the field.

## 1. Introduction

Oxygen reduction reaction (ORR) occurs at the cathode of proton exchange membrane fuel cells (PEMFCs) and rechargeable metal-air batteries, which are attractive for energy storage and conversion applications. PEMFCs convert the chemical energy stored in hydrogen fuels to electricity without producing any pollution making them particularly suitable for transportation, residential power generation, and portable electronic devices. A typical PEMFC operates at low temperature range (50 to 100°C), under ambient pressure, and in highly acidic conditions. In order to improve the efficiency of PEMFCs, Pt-based precious metal electrocatalysts are normally used to promote the kinetic rate of the sluggish ORR. However, the high price and geographic scarcity of Pt hinders the commercialization of PEMFCs. Hence, it is of great interest to find efficient yet durable electrocatalysts which contain no Pt content for ORR.

Among all the alternatives to Pt, metal, nitrogen doped carbon (denoted as M-N-C, M=Fe, Co or Mn) catalysts have exhibited encouraging catalytic performance and been extensively studied.[1-14] The M-N-C catalysts are usually synthesized through high-temperature pyrolysis of the precursors containing transition metal M and nitrogen content, as well as carbon substrate or metal–organic framework. The power density of the membrane electrode assemblies (MEAs) containing Fe-N-C catalysts have approached approximately one third of the performance of those containing the state-of-the-art Pt alloy catalysts.[15, 16] Such results demonstrate the promise of the M-N-C catalysts for future commercial PEMFCs. However, these study[15, 16] also pointed out that the MEA with Fe-N-C catalysts suffered severe degradation at a typical operating condition of PEMFC. Further development of the M-N-C catalysts into a viable alternative to Pt-based catalysts requires fundamental understanding of the chemical nature of the active sites for ORR and the structure-property (i.e., activity and stability) relations of these active sites under PEMFC cathode conditions.

The progresses in the design and synthesis,[17, 18] activity performance,[9, 19] and electrochemical stability[20, 21] of M-N-C catalysts have been recently reviewed. These reviews mainly focus on the survey of experimental studies related to the electrochemical measurements of M-N-C catalysts. By contrast, a critical survey on the progress of computational modeling relevant to the chemical/functional nature of M-N-C catalysts has been largely absent. In particular, many novel, advanced computational methods have been developed and integrated into a cross-cutting

approach to gain mechanistic understanding of the structure-property relations of M-N-C catalysts for ORR, as shown in Figure 1. Consequently, we devote this review to reporting the progresses of computational methods development, and the predictions of the structure-activity and structure-stability relations of the M-N-C active sites. Moreover, this survey aims to summarize how advanced computational modeling accelerates our understanding of the functional mechanisms of the M-N-C electrocatalysts for ORR. Specifically, the computational studies have provided critical knowledge on the chemical nature of active sites, the reaction pathways of ORR on these active sites, and the stability of the M-N-C catalysts.

The article is organized as follows. In section 2, we describe computational modeling approaches commonly used in M-N-C electrocatalyst studies. In section 3, we present the progress of these computational approaches in identifying likely active sites in the heterogeneous, pyrolyzed M-N-C catalysts. In section 4 we review predictions for understanding how active site structures dictate ORR activity using the computational methods. In section 5, we show how related methods can be used to understand the electrochemical stability of atomic scale structures in M-N-C catalysts. Finally, we provide a discussion of the remaining challenges and future directions in the field of computational design of M-N-C electrocatalysts for ORR.

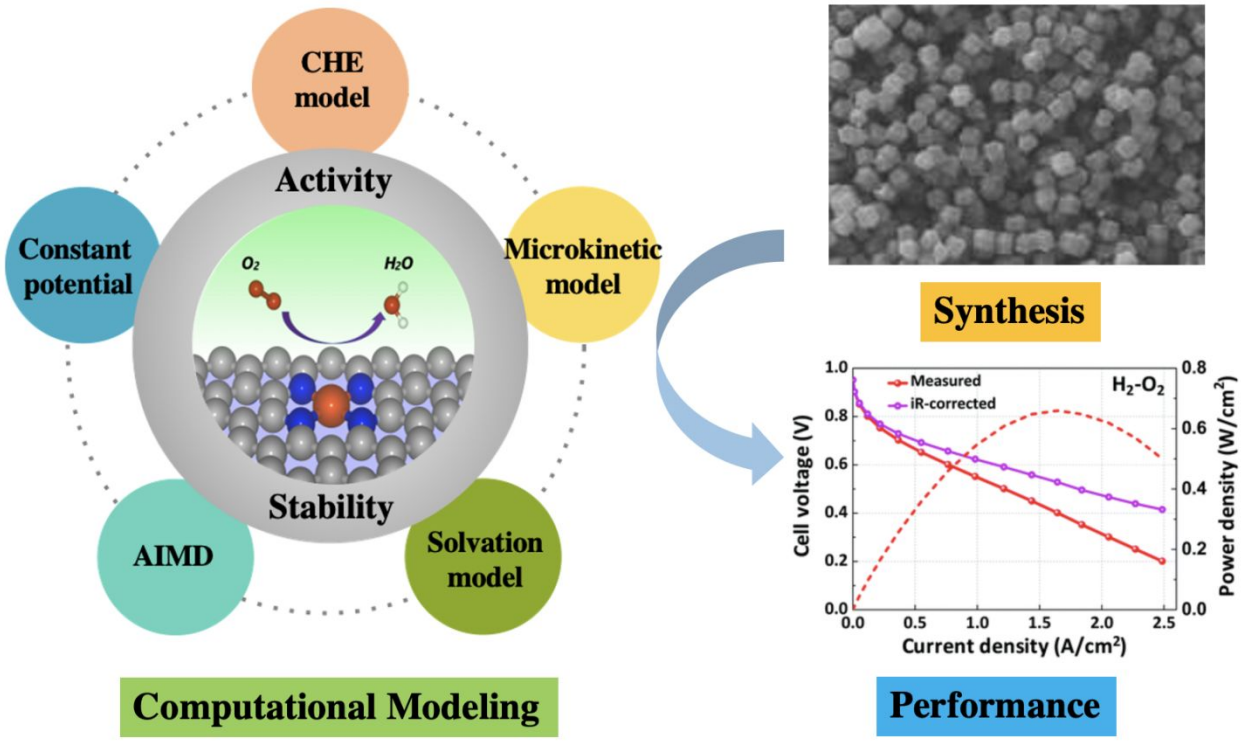

**Figure 1.** Schematic showing how computational modeling has been developed and applied as a cross-cutting approach to understand the complex relation between synthesis and catalytic performance of metal and nitrogen doped carbon materials. Reproduced from Ref.[22, 23] with permission from the Royal Society of Chemistry.

## 2. Computational Methods

### A. Computational hydrogen electrode method

Electrochemical reactions, such as ORR, involve proton-coupled electron transfer steps. To predict the free energies of solvated protons and electrons, Nørskov et al. proposed the computational hydrogen electrode (CHE) method, which has been widely used in computational studies of the thermodynamics of electrochemical reactions.[24] Within the CHE method, the free energy of a proton-electron pair is calculated as shown in Eq. (1)

$$G(H^+ + e^-) = 0.5G_{H_2} - eU_{SHE} - 2.303 \times k_bT \times pH = 0.5G_{H2} - U_{RHE} \quad (1)$$

where $G_{H2}$ represents the calculated free energy of a hydrogen molecule in gas phase under standard condition, $U_{SHE}$ and $U_{RHE}$ represent the applied electrode potential relative to standard hydrogen electrode and reversible hydrogen electrode, respectively, $k_b$ is Boltzmann constant and T is temperature. Here, we use ORR as an example to illustrate the application of CHE for electrochemical reaction study. The associative ORR pathway is shown in Eq. (2).

$$O_2 + 4H^+ + 4e^- + * \rightarrow$$
$$*OOH + 3H^+ + 3e^- \rightarrow *O + 2H^+ + 2e^- + H_2O \rightarrow *OH + H^+ + e^- + H_2O \rightarrow 2H_2O$$
(2)

Considering the relationship in Eq. (1), the free energies of the ORR intermediate states are defined in Eq. (3a-d) and can be expressed as a function of $U_{RHE}$:

$$\Delta G_{O2} = G(O_2) + 4G(H^+ + e^-) - 2G(H_2O) = G(O_2) + 2G(H_2) - 4eU_{RHE} - 2G(H_2O) \quad (3a)$$

$$\Delta G_{OOH} = G(*OOH) + 3G(H^+ + e^-) - 2G(H_2O) = G(*OOH) + 1.5 * G(H_2) - 3eU_{RHE} - 2G(H_2O) \quad (3b)$$

$$\Delta G_O = G(*O) + 2G(H^+ + e^-) - G(H_2O) = G(*O) + G(H_2) - 2eU_{RHE} - G(H_2O) \quad (3c)$$

$$\Delta G_{OH} = G(*OH) + G(H^+ + e^-) - G(H_2O) = G(*OH) + 0.5 * G(H_2) - eU_{RHE} - G(H_2O) \quad (3d)$$

Consequently, the CHE method offers a practical approach to correlate charge-neutral DFT calculations in vacuum to the potential-dependent energetics of an electrochemical reaction. So far, the CHE method has been successfully applied to predict the electrocatalytic activity of metal surfaces.[25] Especially, Greeley et.al used the CHE method to predict a volcano plot of metal catalysts for ORR.[26] They revealed a relationship between the predicted ORR activity and oxygen adsorption energy and thus provided guidance to the development of metal alloy catalysts for ORR.

**B. Solvation models**

Electrolyte solvent is believed to play crucial role in affecting the electrochemical reaction pathway as well as altering the energetics and structures of reaction intermediates.[27-29] Consequently, computational solvation models are needed to capture most significant features of the complex solid/solvent interface in the electrocatalyst study. Several computational approaches have been developed to address this computational challenge. First, a fully explicit solvation model includes all solvent molecules in the DFT calculations. This computational approach gives atomistic insight into the effects of solvation and the effect of electric field on reaction energetics. For example, Goddard et al. have employed forty-nine explicit water molecules (about six layers) to model the solvation effect at the water/Cu(100) interface using quantum molecular dynamics sampling methodology.[30] The shortcoming of the explicit solvation model is that it is computationally very demanding.

In contrast, an implicit solvation model treats the solvation as a continuous media, which can reflect thermodynamic averages of solvation.[31, 32] In the implicit solvation model[33], the total free energy, *A*, of the investigated system containing solute and electrolyte, can be calculated as:

$$A[n(\vec{r}),\phi(\vec{r})] = A_{TXC}[n(\vec{r})] + \int \phi(\vec{r})\rho_s d^3r - \int \epsilon(\vec{r})\frac{|\nabla\phi|^2}{8\pi} d^3r + \int \frac{1}{2}\phi(\vec{r})\rho_{ion}(\vec{r}) d^3r + A_{cav} + A_{ion} \quad (4)$$

where $A_{TXC}$ is the kinetic and exchange-correlation energy from DFT, $\phi$ is the net electrostatic potential of the system, $\rho_s$ and $\rho_{ion}$ are the total charge density of the solute and ion charge density of the electrolyte, respectively, $\varepsilon$ is the permittivity, $A_{cav}$ is the cavitation energy and $A_{ion}$ is the free energy of mobile ion. In the implicit solvation model, the permittivity of electrolyte is used to compute the solvation effect instead of using explicit solvent molecules. Thus, the implicit

solvation model requires less computational resources. However, the implicit solvation model is not ideal for giving atomic level details near the interface and cannot reproduce the chemical interaction of the surface with explicit ions/molecules.

A hybrid solvation model includes some explicit electrolyte molecules near the solid/solvent interface and applies the continuum solvation model at regions far away from the interface. As a result, this computational method can have both accurate atomic level details near the interface and affordable computational cost. Liu et al used the hybrid solvation model with 72 water molecules (6 layers) in conjunction with implicit solution description, to explore the catalytic origin of single Ni-atom in N-doped graphene for $CO_2$ reduction to CO.[34]

**C. Charged reactions and potential**

In some cases, the CHE model fails to predict the correct chemical activity of electrocatalysts due to the limitation of using zero net charge to simulate a charged electrochemical interface.[35] To address this issue of computational electrocatalysis, some efficient computational methods have been developed to simulate the electrochemical reactions under a constant electrode potential. DFT calculations, combined with a grand-canonical ensemble of electrons, have been adopted to predict the system energy as a function of electrode potential. [35-37]

Work function has been proposed to be a good descriptor to define the electrode potential in DFT calculations as follow:

$$U_{SHE} = \frac{\Phi - \Phi_{SHE}}{e} \quad (5)$$

where $U_{SHE}$ is the electrode potential relative to the standard hydrogen electrode (SHE), $\Phi$ is the calculated work function of the investigated system, $e$ is the elementary charge, and $\Phi_{SHE}$ is the work function of SHE, which can be obtained either from experimental data (~4.44 eV)[38, 39] or theoretical calibration (~4.66 eV from CANDLE solvation model)[40]. It should be mentioned that the work function of the catalyst surface relies on the reaction coordinates due to the use of the finite cell size. Currently, there are three methods to tune the work function across the reaction coordinates, namely, cell extrapolation, charge extrapolation, and continuum charging method. In the cell extrapolation method, the cell size is increased to approximate the infinite cell size, at which the overall reaction should operate at constant potential. [41, 42] The charge extrapolation method uses the mean-field approximation to predict the relation between system energy and

potential. [43] In the continuum charging method, the number of electrons can be adjusted to maintain the electrochemical system at specified constant electrode potential, whereas the compensating counter charges were smeared throughout the whole computation cell.[44] Yang et al used the continuum charging method to predict the ethanol oxidation activity of Pd, explaining the formation of various products at the different electrode potential ranges observed in the experimental linear sweep voltammetry curve.[45]

In 2019, Gauthier et.al suggested that the local potential drop between the surface and reaction plane (described by the effective surface charge density) is appropriate to describe the driving force of electrochemical reaction as compared to work function.[27] The effective surface charge density can be computed using the Bader charge analysis[46, 47] of the surface slab and adsorbates. Different from the work function which defines the potential of the overall system, the effective surface charge density gives details about the local potential drop at the interface. Moreover, the computation of the electrochemical interface using the effective surface charge density as a descriptor is independent of the employed cell size or interfacial capacitance. However, the implementation of this descriptor requires an explicit or hybrid solvation model, leading to more expensive computational cost.

**D. Microkinetic modeling**

The prediction of chemical kinetics on catalysts is important in catalysis research. Following the power-law expression[48], the kinetic rate of a reaction can be calculated as:

$$r_i = k_{f,i} * \prod[reactant]^m - k_{b,i}\prod[product]^n \quad (6)$$

where $r_i$ is the kinetic rate of the ith elementary reaction, $k_{f,i}$ and $k_{b,i}$ are the forward and backward rate constants for the ith elementary reaction, symbols *[reactant]* and *[product]* represent the molar concentration of reactants and products, respectively, *m* and *n* are the corresponding exponents for the reactants and products. The forward reaction rate constant can be calculated as:

$$k_{f,i} = A_i \exp\left(-\frac{\Delta G_{a,i}}{k_b T}\right) \quad (7a)$$

whereas the backward reaction rate constant is calculated as:

$$k_{b,i} = A_i \exp\left(-\frac{\Delta G_{a,i} - \Delta G_{f,i}}{k_b T}\right) \quad (7b)$$

where $A_i$ is pre-exponential factor for the ith elementary reaction, $k_b$ is Boltzmann constant, T is temperature, $\Delta G_{a,i}$ is the standard activation energy for the ith elementary reaction, and $\Delta G_{f,i}$ is the free energy change for the ith elementary reaction. Taking $2e^-$ ORR pathway as an example, the reaction rates of all elementary reactions are presented in Table 1. These reaction rates could be determined by solving a system of coupled ordinary differential equations (ODEs), which describe the relation between the time variation of the surface concentration θ of reaction intermediates and the reaction rate of each elementary reaction. These ODEs can be solved at steady state where the surface concentration of each chemical species does not change with time and the total number of surface sites is conserved. After the reaction rates of each elementary reaction are obtained, the current density j of an electrochemical reaction is computed as: $j = e\rho TOF_{e\_}$, where $e$ is the charge of electron, ρ is the surface density of active sites (a typical value of ~$6.8 \times 10^{16}$ sites $m^{-2}$ for M-N-C catalysts[49]), and $TOF_{e-}$ is the turnover frequency of electrons, which is equal to summation of the rates of all the elementary reactions involving electron transfer. Hansen et.al[50] used the microkinetic model to predict a Tafel slope of 59 mV/dec for ORR on Pt(111) surface, in good agreement with experimentally observed Tafel slope (60~88 mV/dec)[51] of Pt catalyst.

**Table 1. Elementary reactions, expression of their reaction rates, and governing equations of 2e- ORR pathway.**

| # | $2e^-$ ORR pathway | Reaction rate | ODEs |
|---|---|---|---|
| 1 | $O_2 + * \rightarrow *O_2$ | $r_1 = k_{f,1} x_{O2} \theta_* - k_{b,1} \theta_{O2}$ | $\frac{\partial \theta_{O2}}{\partial t} = r_1 - r_2$ |
| 2 | $*O_2 + H^+ + e^- \rightarrow *OOH$ | $r_2 = k_{f,2} \theta_{O2} - k_{b,2} \theta_{OOH}$ | $\frac{\partial \theta_{OOH}}{\partial t} = r_2 - r_3$ |
| 3 | $*OOH + H^+ + e^- \rightarrow *H_2O_2$ | $r_3 = k_{f,3} \theta_{OOH} - k_{b,3} \theta_{H2O2}$ | $\frac{\partial \theta_{H2O2}}{\partial t} = r_3 - r_4$ |
| 4 | $*H_2O_2 \rightarrow H_2O_2 + *$ | $r_4 = k_{f,4} \theta_{H2O2} - k_{b,4} x_{H2O2} \theta_*$ | $\theta_* + \theta_{O2} + \theta_{OOH} + \theta_{H2O2} = 1$ |

## E. Computational modeling of M-N-C catalysts

The aforementioned advanced computational methods have been applied to model the activity and stability of varied active sites for ORR in M-N-C catalysts. Typical computational study starts with a proposal of the M-Nx-C atomic structure as active site for ORR, then determines the lowest adsorption configurations of the chemical species involved in ORR (i.e., $O_2$, OOH, O, OH, and $H_2O$) on the proposed M-Nx-C sites using DFT, and further applies the computational hydrogen

electrode method (Section 2.A) to predict the free energy evolution of ORR on the proposed sites. These types of the studies yield the thermodynamic limiting potential for ORR, a descriptor indicating the relationship between structure and corresponding activity. To further improve the accuracy and reliability of the predicted thermodynamic limiting potential for ORR, some studies have included solvation effects (Section 2.B) and electrode potential effect (Section 2.C) in the computational procedures. Integrating both thermodynamic and kinetic computational data, microkinetic modeling (Section 2.D) could predict the half-way potential, a parameter used in experiments to gauge the ORR activity of the M-N-C catalysts, from the calculated polarization curves. Electrochemical stability of M-N-C catalysts can also be considered using DFT methods. In particular, computing the free energy of a dissolution reaction within the CHE framework can indicate regions of (in)stability in pH-potential space. Other deactivation mechanisms such as poisoning can also be quantified based on relative binding energetics. Combined, similar methodologies based on DFT input can provide valuable insight regarding both activity and stability of M-N-C sites.

## 3. Chemical Nature of Active Sites

Early experimental studies revealed a clear correlation between the content of FeNx moieties and the catalytic activity for ORR of the pyrolyzed Fe-N-C catalysts.[52] However, it was difficult to identify the chemical nature of the active sites for ORR in M-N-C catalysts. Complementary to experimental effort, the first-principles computational methods have been used to predict the ORR activity on various possible M-Nx moieties embedded in carbon layers. As depicted in **Figure 2(a)**, many M-$N_x$ moieties with a single transition metal atom coordinated with the number of N atoms ranging from one to four and embedded in a graphene layer have been investigated for their ORR activity. It is particularly relevant to use the first-principles calculations for prediction of the adsorption energy of chemical species involved in ORR on the M-Nx sites with varying chemical structures. The adsorption energy is defined as the energy difference between the adsorbate system and the corresponding isolated systems. In order to be an efficient active site for ORR, the M-Nx sites should at least be able to adsorb reactant $O_2$ molecule on the site to initiate the reaction and easily desorb product $H_2O$ from the site to complete the reaction. Table 2 summarizes the calculated adsorption energies of $O_2$ and $H_2O$ gas molecules on various FeNx sites from the literature. [53-56] It can be found that the $O_2$ adsorption energy are all predicted to be negative on

FeNx (x=1 to 4) sites, suggesting favourable $O_2$ adsorption on these sites. However, the adsorption energies of $H_2O$ on $FeN_1$, $FeN_2$ and $FeN_3$ sites are predicted to be strongly bound by more than -0.4 eV, which is the solvation energy of $H_2O$ gas molecule in aqueous electrolyte[57]. As a result, product $H_2O$ from ORR would be difficult to desorb to free the sites for the next reactions. In contrast, the two $FeN_4$ sites are predicted to have appropriate binding strength with $O_2$ and $H_2O$ gas molecules comparable to that on Pt (111) and hence be the active sites for ORR in Fe-N-C catalysts from the computational studies.

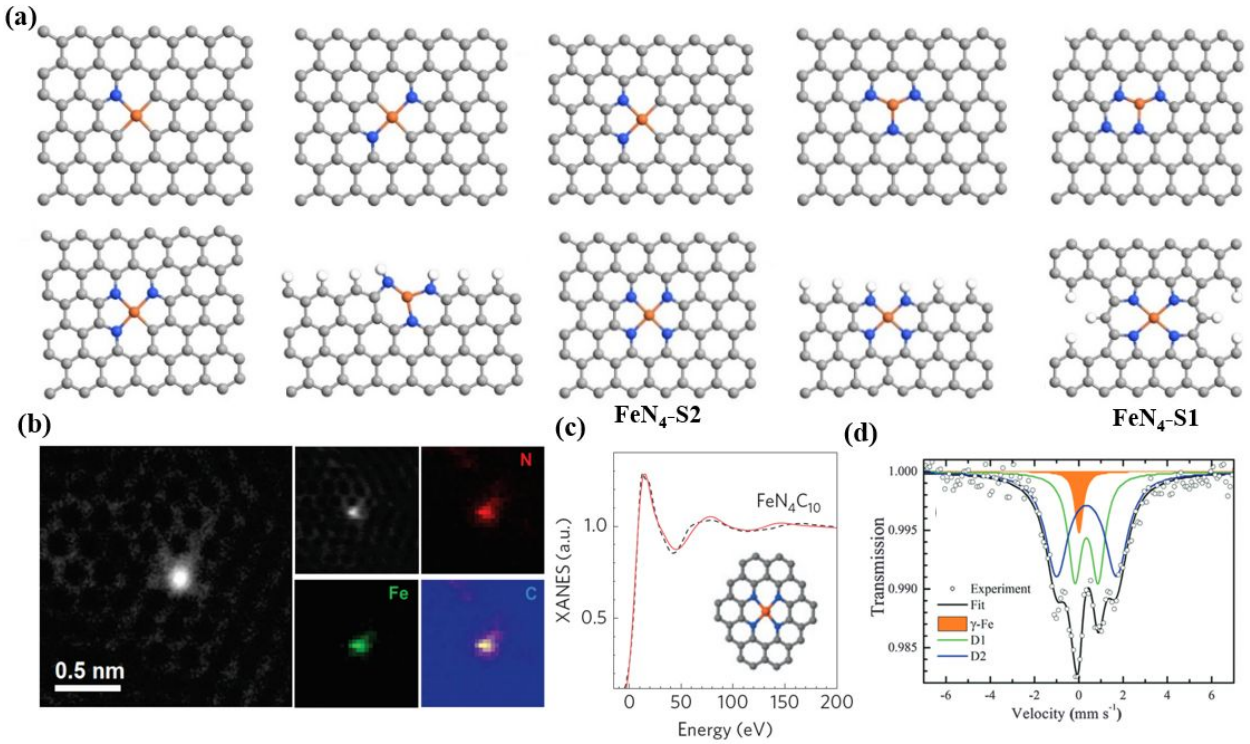


**Figure 2.** (a) Atomistic structures of various M-Nx moieties in a graphene layer.[58] The grey, blue, and orange balls represent carbon, nitrogen and transition metal atoms, respectively. Notable experimental characterization results of ORR active sites in M-N-C catalysts from (b) HAADF-STEM images with EEL spectrum from Ref [59]. Reprinted with permission from AAAS. (c) K-edge XANES spectrum. Adapted with permission from Ref [60]. Copyright 2015 Nature. and (d) room temperature Mössbauer absorption spectrum. Reproduced from Ref. [61] with permission from the Royal Society of Chemistry.

**Table 2. Predicted adsorption energies of $O_2$ and $H_2O$ gas molecules on various $FeN_x$ sites and Pt(111). Negative value of adsorption energy indicates attractive interaction between $O_2$ (or $H_2O$) and the sites.**

| $E_{ad}$ (eV) | $O_2$ | $H_2O$ | reference |
|---|---|---|---|
| $FeN_1$ | - 1.94 | - 0.73 | [53] |
| $FeN_2$ | - 1.67 | - 0.47 | [54] |
| $FeN_3$ | - 2.48/-3.17 | -0.90/-0.80 | [56,54] |
| $FeN_4$-S1 | -0.63 | -0.27 | [55] |
| $FeN_4$-S2 | -0.98 | -0.18 | [54] |
| Pt(111) | - 0.13 | - 0.27 | [54] |

The computational prediction that $FeN_4$ moieties embedded in carbon layer are active for ORR has been largely validated by catalyst characterization studies. As shown in Figure 2(b), Chung et.al employed high-angle annular dark-field scanning transmission electron microscopy (HAADF-STEM) to characterize the structure of Fe-N-C catalyst with remarkable activity and directly observed dispersed sites containing a single Fe atom surrounded by four N atoms in average in the catalysts. [59] The $FeN_4$ moieties was further identified in Fe-N-C catalysts through comparing the K-edge X-ray absorption near edge structure (XANES) measured and theoretical spectrum calculated for a $FeN_4$ site (Figure 2(c)) [60, 62]. Recently, Jaouen et al. distinguished two types of $FeN_4$ sites in Fe-N-C catalysts with Mössbauer spectroscopy (Figure 2(d)), namely high-spin S1 type $FeN_4$ site and the low- or intermediate-spin S2 type $FeN_4$ site.[63] It should be noted that the two $FeN_4$ sites were attributed to having different local carbon structures, as shown in Fig. 1a. It should be noted that the computational and experimental studies also show that $MnN_4$, $CoN_4$ and $NiN_4$ moieties are the active sites for ORR in Mn-N-C, Co-N-C and Ni-N-C catalysts.[3, 13, 64-66]

The same or similar M-$N_4$ (M=Fe, Co, Mn) moieties can be found in transition metal porphyrins and transition metal phthalocyanines, which have also be found to promote ORR which inspired initial work toward heat-treated M-N-C electrocatalysts.[67] The electronic structure of the central

transition metal in these heterocyclic macrocycle molecules have been extensively studied using DFT methods. As elaborated by Jean et.al, the $3d_{x2-y2}$, 4s, $4p_x$, and $4p_y$ orbitals of the central M atom in the square, planar M-$N_4$ with a $D_{4h}$ symmetry group would form four σ-type metal-ligand bonds with the four chelated N atoms, whereas the other orbitals including $3d_{xy}$, $3d_{yz}$, $3d_{xz}$, and $3d_{z2}$ would transform into four non-bonding d-type molecular orbitals to interact with the surface adsorbates.[68] As a result, the catalytic activity of the M-$N_4$ moieties is believed to be strongly related to the energy level of these four non-bonding *d*-type molecular orbitals of the central metal. [69] It is conceivable that the same understanding is applicable to the M-$N_4$ sites as identified in M-N-C catalysts active for ORR.

## 4. Activity Predictions

On the surface of catalysts, ORR could proceed through either two- or four-electron pathway. Following a two-electron pathway, the oxygen adsorbed on the catalysts will be reduced to hydrogen peroxide without breaking the O-O bond in $O_2$. In contrast, the oxygen adsorbed on the catalysts will be reduced to water following a four-electron pathway which requires a O-O bond scission process. For high energy conversion efficiency and membrane stability, four-electron ORR pathway is more desirable in PEMFCs as compared to two-electron ORR. Depending on how the O-O bond scission occurs, the four-electron ORR can be further distinguished by three possible pathways[70]: in a $O_2$ dissociation pathway, the O–O bond scission step occurs through direct dissociation of the bound $O_2$; in a OOH dissociation pathway, the adsorbed $O_2$ will be first protonated to form OOH and then the O–O bond scission step is accomplished by the dissociation of OOH into O and OH; and in a hydrogen peroxide dissociation pathway, the OOH will be further protonated to form $H_2O_2$ and then the O–O bond scission proceeds through the dissociation of $H_2O_2$ into two OH.

Many DFT computational studies have been performed to predict the molecular details and free energy evolution of various ORR pathways on the M-$N_4$ sites embedded in carbon layer.[71-73] These computational studies indicate that both two-electron and four-electron ORR pathways are possible on a M-$N_4$ site mainly depending on the element type of the central M, consistent with experimental observations of product selectivity. As shown in **Figure 3(a)** (blue dash line), the two-electron pathway for ORR on a M-$N_4$ site initiates from the adsorption of $O_2$ molecule on the central M, then the adsorbed $O_2$ is protonated to form OOH and $H_2O_2$ sequentially on the central

M, and the produced $H_2O_2$ desorbs into electrolyte. In contrast, following a four-electron pathway for ORR in **Figure 3(a)** (brown dash line), the $O_2$ molecule will first adsorb on the central M, this adsorbed $O_2$ will further be reduced to form *OOH on the central M, the *OOH will dissociate into *O and *OH, and two $H_2O$ molecules will be produced and desorb into electrolyte. To model these ORR process on a M-$N_4$ site in a computational study, the protons involved are normally assumed to come from the explicit solution of electrolytes and the electrons needed are from a conductive electrode, respectively (**Figure 3(b)**).

Several computational approaches have been developed and applied to predict the activity of the M-$N_4$ sites for ORR. The widely employed approach is to calculate the free energy evolution of ORR on thee M-$N_4$ sites using the computational hydrogen electrode method as described in Section 2.[74-76] The free energy evolution for ORR can be obtained by plotting the free energy of all the chemical species involved in ORR following their occurrence order in a given pathway as shown in **Figure 3(a)**. The highest electrode potential under which all of the free energy changes along the ORR pathway are exergonic is thus defined as the thermodynamic limiting potential for ORR on the M-$N_4$ sites. The kinetic barrier for each elementary reaction is normally considered to scale with the free energy change of the reaction.[77] Exner et.al computationally examined both the thermodynamic and kinetic data of some electrochemical reactions and found that the predictions based on thermodynamic free energy evolution agreed well with those from ab initio kinetics for ORR on Pt(111). [78] This result suggests that the thermodynamic limiting potential should show a same trend with the kinetic onset potential for ORR activity. Namely, high limiting potential indicates high ORR activity of the catalysts. For example, the computational results from Liu et. al indicated that the S1 type $FeN_4$ site exhibited a higher ORR limiting potential of 0.68 V than that (0.62 V) of the S2 type $FeN_4$ site **(Figures 3(c) and 3(d))**,[55] indicating that the S1 type $FeN_4$ site should be more active for ORR than the S2 type $FeN_4$ site. This computational prediction is in good agreement with the recent experimental finding.[63] Moreover, the ORR limiting potential on a $FeN_4$ site with a OH adsorbed on the other side, which is believed to occur under high electrode potential, was calculated to have a higher limiting potential of 0.76 V,[79] even closer to experimentally measured ORR onset potential. In addition, $MnN_4$ and $CoN_4$ sites were reported to exhibit a high ORR activity with a limiting potential of 0.54 V and 0.67 V, respectively.[3, 22] These predictions are consistent to the experimentally observed ORR activity trend following a descending order of Fe-N-C, Co-N-C, and Mn-N-C.[6, 80] These DFT predictions provide good

explanation to experimental observation that M-$N_4$ (M=Fe, Co, Mn) sites (Figure 3(c)) are active for ORR. In comparison, both $NiN_4$ and $CuN_4$ sites were predicted to have a limiting potential below 0.1 V, in line with the observed inferior ORR activity of Ni-N-C and Cu-N-C catalyst in acid media.[81] It should be noted that M-$N_4$ containing metalloporphyrin was also predicted to show activity for ORR.[82, 83] For example, Co-porphyrin and Fe-porphyrin have been predicted to have a limiting potential above 0.60 V for ORR, whereas Ni-porphyrin and Cu-porphyrin are not active to promote ORR.[82] Moreover, the catalytic activities of the transition metal macrocyclic complexes for ORR were proposed to be positively related with the ionization potential and the $O_2$ binding ability.[84]

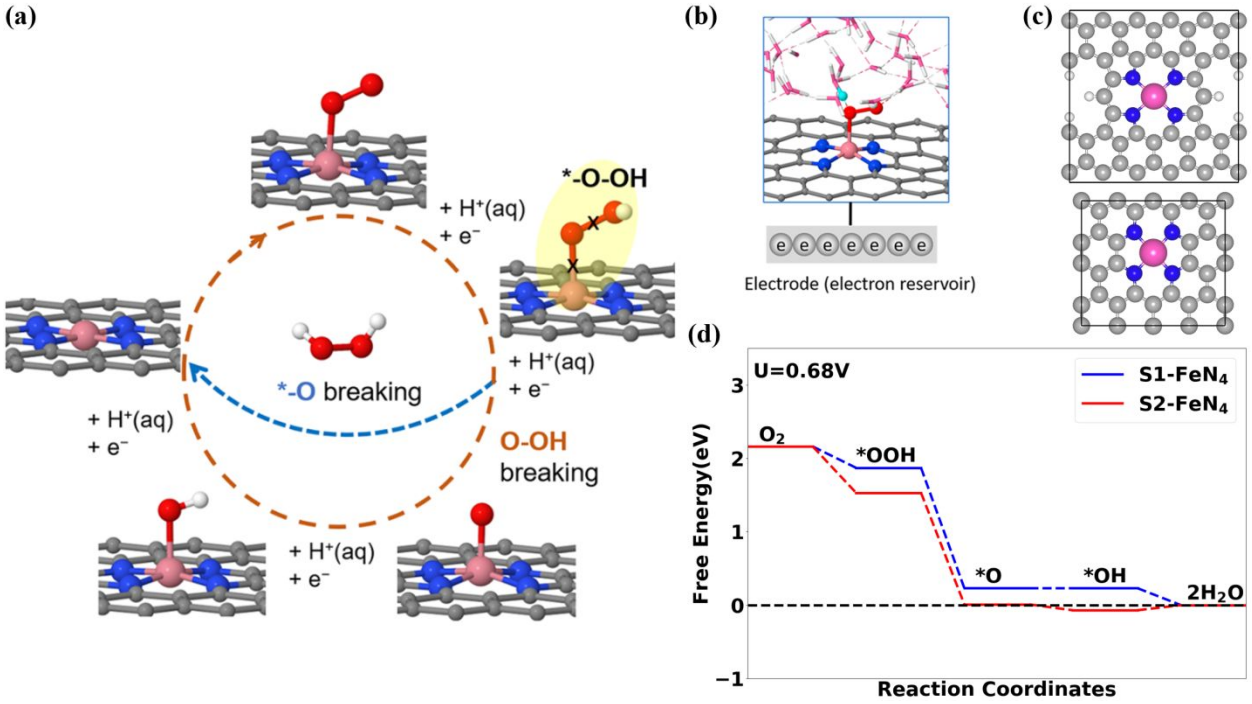


**Figure 3.** (a) Schematics of possible pathways for ORR on a M-$N_4$ site embedded in a graphene layer. Adapted with permission from Ref. [34]. Copyright 2020 American Chemical Society. (b) Atomistic structures of the employed calculation model including a graphene containing an in-plane M-$N_4$ site, adsorbed OOH, and explicit water environment. Adapted with permission from Ref. [34]. Copyright 2020 American Chemical Society. (c) Atomistic structures of S1 type (top) and S2 type (bottom) M-$N_4$ sites active for ORR (d) Calculated free energy evolution for ORR on a S1 type and a S2 type $FeN_4$ sites following a $4e^-$ OOH dissociation pathway under an applied electrode potential of 0.68 V. Plot (d) is replotted based on the data from reference[55]. In the figure, the grey, blue, pink, red, and white balls represent C, N, metal, O, and H atoms, respectively.

Despite much success, some discrepancies between computational predictions and experimental measurements still exist. For example, Zhong et al. reported that the experimental half-wave potential for ORR of Fe-N-C catalyst in alkaline (i.e., 0.916 V/RHE) was significantly higher than that in acid (i.e., 0.748 V/RHE) and neutral media (i.e., 0.792 V/RHE), revealing significant pH-dependent ORR performance of the Fe-N-C catalyst.[85] Failing to model the pH-dependent activity of M-N-C catalysts, the typical CHE computational method employs a metal/vacuum interface at zero charge to simulate a charged electrochemical interface at a constant potential and thus cannot account for the variation of the adsorption energy of chemical species as a function of pH value. In addition, accurate predictions of the experimental observables such as onset potential, half-wave potential, and Tafel slope are absent in the computational studies of M-N-C catalysts for ORR. The experimentally measured ORR halfwave potential of Fe-N-C catalyst was reported to be 0.91 V[86], quantitatively different from that of 0.68 V predicted from theoretical calculation using the CHE method.[87] These discrepancies between computational predictions and experimental measurements are expected to be resolved by application of a constant potential based computational method (See Section 2C) which was developed to model the charged electrochemical reactions. It should be mentioned that such computational method has been demonstrated to be capable of revealing the pH-dependent ORR activity on Au(100) surface[35], and giving accurate predictions on the onset potential of CO oxidation reaction on Au(111) surface[88] and the Tafel slope of oxygen evolution reaction on $IrO_2$(110) surface[89]. Consequently, the constant potential based computational method should be applied to model the activity of M-N-C catalysts for electrochemical ORR.

Furthermore, the spin state of the system, which could affect the adsorption energy of ORR intermediates on M-N-C catalyst [90], is not fully explored in the current literature. In an only study in this regard, Duan et al.[91] have applied an occupation matrix control methodology[92] to tune the spin state of chemical adsorption on $CoN_4$ site and predicted *OH should have a the high-spin state and *O have an intermediate-spin state under -0.8 to 1.2 V/SHE electrode potential, whereas *OOH would have a low-spin state under -0.8 V to 0.06 V/SHE and an intermediate-spin state under 0.06 V to 1.2 V/SHE. Mineva et al. combined experimental approaches and DFT modeling to determine likely spin states of Fe in synthesized Fe-N-C systems and concluded the essence of low-spin Fe(II) and high-spin Fe(III) states.[93] Variations were attributed to differences in local carbon structure. He et al. reported DFT simulations that show how a local Cu atom could impact

the magnetic moment of Fe in Fe-N-C which in turn modified calculated *OH binding and thus ORR activity.[94] Sun et al. used DFT calculations to determine that Fe spin state in Fe-N-C complexes directly impacts not only activity but also stability against metal dissolution.[95] These results indicate clearly that the spin state of the system should be considered for prediction of the ORR activity of M-N-C catalysts as a function of applied electrode potential in future modeling studies.

Another type of computational approach is to calculate the kinetic activation energy for O-O bond scission process on the M-$N_4$ sites using the nudged elastic band (NEB) method. Due to a high dissociation energy of O-O bond in oxygen molecule (~500 kJ/mol at 298K) [96], the capability to efficiently break O-O bond plays a vital role to promote four-electron ORR. Generally speaking, the O-O bond scission process with an activation energy lower than 0.90 eV is kinetically feasible on the catalysts surface at 300K.[48] As mentioned above, there are three possible non-electrochemical ways to break the O-O bond of $O_2$ molecule adsorbed on a M-$N_4$ site, namely, $O_2$ dissociation (**Figure 4(a))**, OOH dissociation (**Figure 4(a))** and $H_2O_2$ dissociation. Using the NEB computational method, Liu et al predicted that the $O_2$ dissociation required an unsurmountable activation energy of 1.19 eV on an S2 type $FeN_4$ site and 1.96 eV on an S2 type $CoN_4$ site[97], respectively, implying direct $O_2$ dissociation might not be feasible on these M-$N_4$ sites. Alternatively, the OOH dissociation, in which an OOH adsorbed on the central M breaks into a O adsorbed on M and a OH adsorbed on an adjacent active carbon (as shown in **Figure 4(a)),** was predicted to require overcoming a low energy barrier of 0.56 eV on $FeN_4$ site and 0.37 eV on $MnN_4$ site, suggesting that $FeN_4$ and $MnN_4$ sites are able to efficiently promote four-electron ORR via the OOH dissociation path. These computational predictions agree well with experimental findings that Fe-N-C and Mn-N-C catalyst shows a high selectivity toward $4e^-$ ORR pathway[3, 16]. It should be noted that Wang et al computationally showed that the OOH dissociation could also occur through a proton-coupled electron transfer pathway with the assistance of explicit water electrolytes. [79] Electrochemically, the activation energy for the OOH dissociation step on $FeN_4$(OH) sites was predicted to be 0.17 eV (Figure 4(b)).[79] Therefore, the OOH dissociation step on $FeN_4$ was predicted to be kinetically facile through both non-electrochemical and electrochemical routes, thus enabling the desired $4e^-$ ORR pathway in Fe-N-C catalysts. It is noted that the kinetic rate of the OOH dissociation depends on both the activation energy and a pre-exponential factor. As pointed out by Hansen et al, [50] the pre-exponential factor for non-electrochemical OOH

dissociation reaction is significantly higher than that for electrochemical OOH dissociation reaction on Pt(111) surface. Therefore, a direct comparison of the values of the calculated activation energies from different dissociation routes (electrochemical vs. non-electrochemical) in M-N-C catalysts should also be avoided.

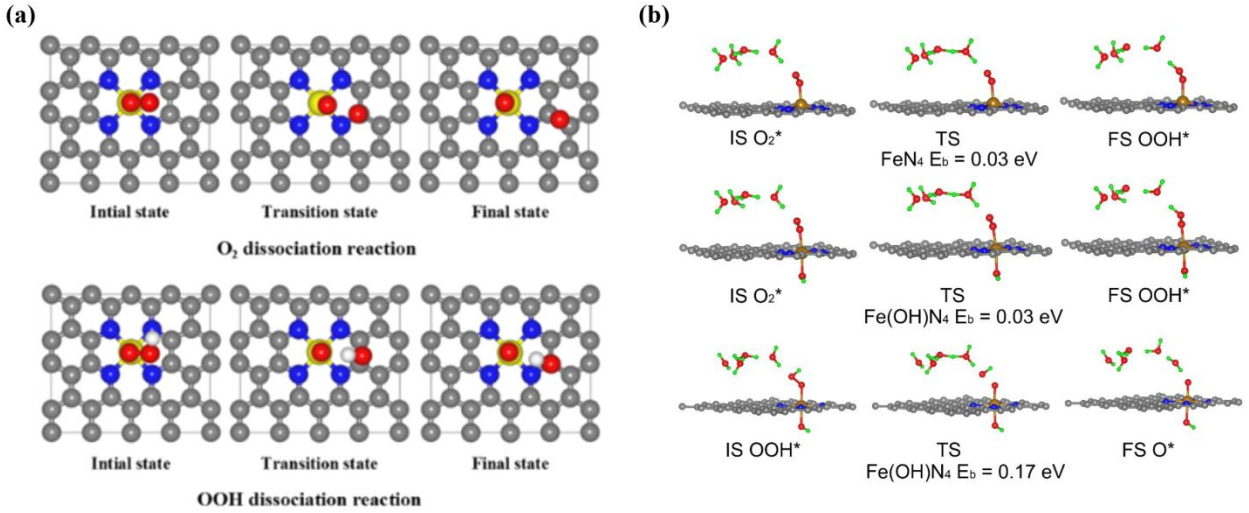


**Figure 4.** Atomistic structures of the initial state, transition state, and final state for (a) non-electrochemical $O_2$ dissociation and OOH dissociation reaction on a $FeN_4$ active site embedded in a graphene layer. Adapted with permission from Ref. [97]. Copyright 2016 American Chemical Society., and (b) $O_2$ protonation reaction on a $FeN_4$ site, $O_2$ protonation reaction on a $FeN_4$(OH) site, and OOH dissociation reaction on a $FeN_4$(OH) site in explicit water environment. Adapted with permission from Ref. [79]. Copyright 2019 American Chemical Society. In these figures, the grey, blue, yellow, red, and white (or green) balls represent C, N, Fe, O, and H atoms, respectively.

In comparison, no consensus has been achieved regarding the selectivity of Co-N-C catalyst for ORR. [22, 97-101] In experiments, Gao et al. reported that the Co-N-C catalyst synthesized through pyrolysis of melamine with L-alanine exhibited an over 90% $H_2O_2$ production (i.e., favoring $2e^-$ ORR)[98]. By contrast, the Co-N-C catalyst derived from ZIF-8 precursors was found to show a high selectivity toward $4e^-$ ORR with $H_2O_2$ yield below 7.5%[22]. The computational studies suggest that the selectivity of $CoN_4$ sites for ORR is strongly related to the local chemical structure of the active sites. The activation energy for the OOH dissociation on an S2 type $CoN_4$ site was predicted to be 1.11 eV,[97] high enough to prevent the $4e^-$ ORR. In addition, Liu et al. compared the calculated activation energies for the competing OOH dissociation and OOH desorption processes on the S2 type $CoN_4$ site and predicted that the kinetically facile OOH desorption process would primarily

lead to $2e^-$ ORR.[101] As shown in Figure 3(c), the S2 type $CoN_4$ site contains a $CoN_4$ moiety embedded in an otherwise intact graphene layer. Modifying the local carbon structure, a $CoN_{2+2}$ site is hosted by micropores and bridges two adjacent armchair-like graphitic edges.[22] The activation energy for the OOH dissociation on a $CoN_{2+2}$ site was calculated to be only 0.69 eV, low enough to permit the $4e^-$ ORR to occur on this site. Moreover, Jung et al reported that the selectivity of the S2 type $CoN_4$ site could change from $2e^-$ to $4e^-$ ORR if the carbon atoms adjacent to nitrogen of the $CoN_4$ moiety are oxidized.[100] Similarly, the O-O bond breaking reaction was reported to be unfavorable on Co macrocyclic complexes leading to $2e^-$ ORR, but favorable on Fe macrocyclic complexes leading to $4e^-$ ORR.[11] Sun et al attributed this trend to a higher energy level of $e_g$ (HOMO) orbital of Fe phthalocyanine than that of Co phthalocyanine.[102]

The microkinetic modeling computational method has also been employed to predict the activity of M-$N_4$ sites for ORR. Specially, the microkinetic modeling for ORR considers multiple elementary steps, including $O_2$ diffusion, $O_2$ adsorption, various surface reactions, and product desorption. As described in Section 2D, the microkinetic modelling predicts the output current density of ORR as a function of applied electrode potential (i.e., polarization curve) and hence produces computational results that can be directly compared with the experimental measured linear sweep voltammetry (LSV). Using the microkinetic modeling, Liu et.al[87] predicted that the half wave potential of ORR on a $FeN_4$ site was about 0.02 V higher than that on a Pt (111) surface, consistent with the recent finding of Fe-N-C catalysts yielding high ORR activity comparable with Pt in acids. [103] In another microkinetic modeling study, Wang et al[79] predicted the half wave potential of ORR to be 0.88 V, 0.85V and 0.73 V on $FeN_4$, $CoN_4$, and $MnN_4$ site, respectively. It appears that the computational predictions agree well with the experimentally measured value of 0.89 V on Fe-N-C[6]. 0.82 V on Co-N-C[22], and 0.80 V on Mn-N-C catalysts[3, 87]. Moreover, microkinetic modeling gives information about the evolution of surface coverage of various chemical species involved in ORR on the catalyst surface which is a major advantage over other computational approaches. In this regard, the microkinetic modeling predicted that the $FeN_4$ sites would be covered by absorbate OH under the electrode potentials in the range from 0.4 to 0.8V.[59] This prediction can explain the observed experimental redox peak near 0.7 V in cyclic voltammetry of Fe-N- C catalyst.[104]

## 5. Stability Predictions

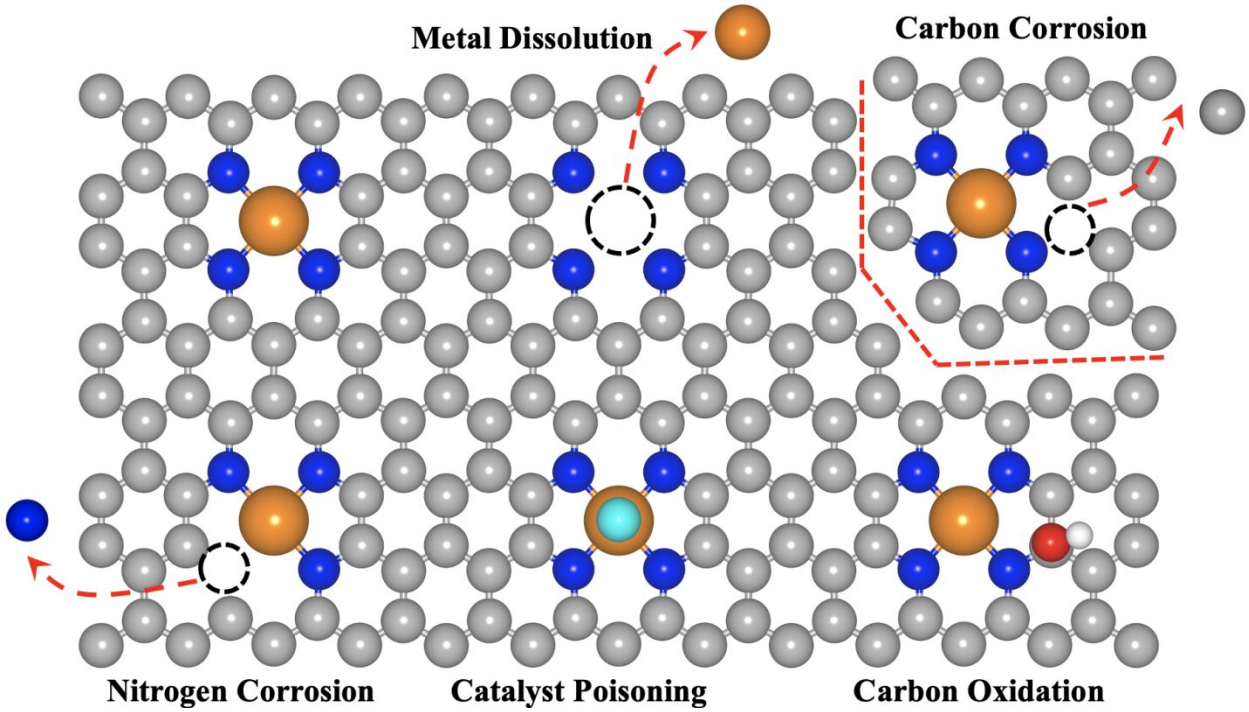


Figure 5. Schematics of various degradation mechanisms on M-$N_4$ site. In this figure, the grey, blue, orange, red, cyan and white balls represent C, N, Metal, poison, O, and H atoms, respectively.

Understanding how activity is declining during ORR, i.e., the stability of the electrocatalyst under even static *in situ* conditions, is a topic of growing importance in the platinum group metal (PGM)-free ORR electrocatalyst community.[20, 21] It should be noted that M-N-C catalysts were reported to have a superior ORR durability than macrocyclic catalyst.[3, 16, 105, 106] Computational modeling of M-N-C electrocatalyst active site stability during ORR has taken a variety of approaches. Early efforts focused on relative thermodynamic stability of varied active site structures with reference to lone-metal or bulk-metal reference states.[107] While the formation energy values that resulted are valuable for qualitatively comparing the relative stability of possible sites, the ubiquitous pyrolysis steps used in synthesis that imbue higher ORR activities suggests that realized active sites are in fact metastable. More recent approaches for understanding stability focused on specific degradation mechanisms. As depicted in Figure 5, the proposed activity loss mechanisms include[108]: dissolution of the central metal atom in the active sites under acidic environments such as PEMFC cathodes; local N- and C-degradation which may alter the local electronic structure and binding energetics and therefore impact calculated activity pathways or promote further degradation; local poisoning of the active site center itself or of the local C

environment, serving to sterically block the active site; and finally, ionomer degradation/repartitioning that strands given active sites, starving them of access to reactant protons.

Thermodynamic stability descriptors for M-N-C catalysts are most often obtained through treating ORR active sites as defects in a host carbon matrix and calculating the defect formation energetics based on assumed reference state values using DFT method. Kattel et al. published a series of studies exploring formation energetics, among other attributes, of Co-$N_x$, Fe-$N_x$, and Ni-$N_x$ structures hosted in basal plan graphene (and armchair edge graphene for the latter).[109-111] They predicted that the 4-fold N coordination vs. 2-fold N coordination of metal sites was energetically favorable and that metal reference state (lone atom vs. bulk metal) influenced the endo- vs. exothermic nature of the defect formation enthalpy. The 4-fold N coordination was later confirmed to be the most probable by comparing the formation energy of Fe with 0, 1, 2, 3, and 4 fold N coordination.[74] Moreover, Holby and Taylor used DFT and semi-empirical potentials to explore how embedded 3-fold coordinated N monovacancy-based Fe sites and 4-fold coordinated N divacancy-based Fe sites compared energetically with a focus on local position of the carbon with respect to a graphene edge.[112, 113] Additionally, studies of defect clustering at the edge[114] as well as spontaneous ligation[115] were pursued by this group. Combined, these studies gave important input regarding likely active site structures. The relatively high thermodynamic stability of in-plane, 4-fold N-coordinated Fe in particular remains a key aspect of most model sites considered today, though a more complete treatment of degradation processes is required to understand the chemical nature of stability.

ORR in a PEMFC cathode takes place under extreme conditions of low pH, high electrode potential, and elevated temperature. In such environments, bulk metal Fe is itself not stable and previous thermodynamic treatments with positive formation energies when a bulk Fe metal reference state is used suggests that Fe-N-C structures are also unlikely to be stable under low pH/high potential conditions. Furthermore, Fe and other proposed transition metal atoms dissolve to cations which thus serve as a more appropriate reference for dissolution. One study considered some environmental effects on active site stability[116] and focused on identifying dissolution of Fe atoms from given atomic structures using a non-electronic-structure-based thermodynamic model. They predicted that for the proposed dissolution reaction, $FeN_4$ structures were stable against dissolution, largely due to entropic stabilization. Using integrated DFT-derived values and

modified treatments of ionic dissolution products, Holby et al. [117] found that for a limited set of proposed dissolution reactions, passivation may help to stabilize Fe-N-C structures in PEMFC relevant pH and potential ranges. They proposed the use of computational Pourbaix-like diagrams with limited considered phases to address the dissolution of given (possibly metastable) structures. With additional considered reactions and varied DFT-approach, Patniboon and Hansen showed[118] that for a variety of central metal species and varied local carbon structures, such sites were in general not thermodynamically stable against dissolution in PEMFC relevant pH and potentials, though they suggest the kinetics of dissolution may aid in stabilizing sites beyond the thermodynamically defined limits. They further suggested a stability descriptor for dissolution based on the free energy of the dissolution reaction for the most stable solid phase (generally the *O or *OH ligated structures). Pourbaix diagrams graphically describe relative stability of various thermodynamic states of the M-$N_4$ active sites as a function of pH value and electrode potential in electrolytes. Consequently, Pourbaix diagrams have been shown to be a valuable computationally-accessible tool for understanding the thermodynamic conditions under which metal dissolution would occur in M-N-C catalysts.

Other computational studies focused on understanding the possible metal dissolution reaction pathways including likely kinetic barriers.[99, 119] Wang et al proposed a possible metal dissolution pathway for M-$N_4$ sites could be considered as a process in which the central metal ion moves away from the 4-fold N coordination (active for ORR) to a 2-fold N-coordination structure (inactive for ORR), while the other two nitrogen are passivated by protons from electrolyte. [99, 119] Using the calculated free energy changes for this metal dissolution pathway, they predicted that the adsorption of gas $O_2$ molecule on the M-$N_4$ (M= Fe, Co, and Mn) sites could greatly reduce their stability against metal dissolution. This computational prediction provides one possible explanation as to why M-N-C catalysts are subject to more severe metal dissolution in oxygen-containing environment. Moreover, from the calculated free energy changes for the assumed metal dissolution pathway they predicted that $CoN_4$ sites would exhibit higher resistance to metal dissolution than $FeN_4$, agreeing well with the trend observed experimentally. Aiming to gain kinetic information of metal dissolution, Wang et al. further viewed the overall metal dissolution process on $O_2$ ligated $FeN_4$ sites to have three sequential steps. The two N in $FeN_4$ site are first protonated, then the $O_2$-ligated central Fe ion will move away from the N4-coordination to an inactive N2-coordination, and lastly the $O_2$-ligated Fe (Fe-O2) will desorb from the catalyst surface.

Analyzing the calculated activation energies for these three steps, they predicted that the nitrogen protonation step was the rate-determining step of metal dissolution, in line with the results from Ab Initio molecular dynamics results[120]. Interestingly, these kinetic calculations predicted that the S2 type $FeN_4$ site exhibited higher stability against metal dissolution than S1 type $FeN_4$ site, consistent with experimental measurements. [16]

In addition to the central transition metal, carbon structures that make up the support/host for ORR active sites in M-N-C catalysts are also not thermodynamically stable under *in situ* conditions and are known to be only kinetically stable. Despite this known instability, relatively fewer atomic scale modeling work has been performed to understand how the C and N atoms surrounding imbedded transition metal atoms impacts overall stability of the M-$N_4$ sites. One study[121] suggested the use of a TEM beam damage model for understanding relative C-structure stability. As the corrosion of C in particular is known to be kinetically limited under fuel cell relevant conditions, this method uses *ab initio* molecular dynamics to probe the input kinetic energy to break all bonds for given atoms in particular structures (threshold energy). This approach is being extended at present to include the roles of Fe-N-C structures and to explicitly include temperature effects. Local C-structure has a significant impact on calculated threshold energies of beam damage which implies that the kinetics of bond breaking of N/C in varied sites are different. This in turn suggests that the stability of N in particular around different sites (even so called $FeN_4$ sites which can have different local carbon environments[55]) have varied C/N corrosion susceptibility. It should be noted that the previous metal dissolution and local C/N corrosion have only been applied to idealized structures and may be difficult to distinguish experimentally in a heterogeneous material. It is also possible that either initial metal corrosion leads to enhanced C/N corrosion or that C/N corrosion can lead to subsequent metal dissolution which further hampers experimental exploration of dominant activity loss mechanisms. While further work is required, probe threshold energy studies provide a valuable kinetic descriptor tool to evaluate C/N stability as a function of local atomic structure.

Finally, the poisoning of PGM-free ORR active sites may also be a degradation pathway. Unlike Pt surfaces, these M-$N_4$ sites are generally more robust against small molecule poisons such as CO. The possibility of poisons and/or intermediates to bind on both the underside and topside of edge hosted or basal plane hosted structures has in fact been suggested as a strength of some M-N-C active sites, allowing for one side to be ligated (not poisoned, perse), leading to

improved activity for overbinding sites, and leaving an additional site free to perform ORR. ORR intermediate OH was the initially proposed ligation moiety[59, 115] for Fe-N-C structures, highlighting another key difference between these sites and Pt-alloy nanoparticle sites which can be poisoned by OH. Svane *et al.*[122] used DFT calculations to show which poisons may act as ligands in M-$N_4$ systems, with a single binding, and which would double-bind, blocking two sites likely acting as a more classical poison. Additional studies, particularly those that aid in the interpretation of active site quantification through poisoning/stripping, are needed to better understand what environmentally relevant molecules may serve to ligate or poison active sites.

## 6. Summary and Perspectives

The development and application of the first principles based computational methods for electrocatalysis indeed accelerate the understanding of the chemical nature of the active sites for ORR, the evolution of chemical species during ORR, and the structural/chemical degradation processes of metal, nitrogen doped carbon catalysts. Some notable computational modeling results include single metal M-$N_4$ (M=Fe, Co, and Mn) sites embedded in a carbon layer are active for promoting ORR, especially $FeN_4$ and $MnN_4$ sites could promote four-electron ORR through efficiently breaking the O-O bond of OOH, the S1 type $FeN_4$ has higher ORR activity but less stability than the S2 type $FeN_4$, and $CoN_4$ is predicted to be more stable than $FeN_4$ site during ORR.

Despite of much success, novel computational methods are still urgently needed to address some challenging questions related to the synthesis and utilization of M-N-C catalysts for PEMFCs. For example, no convincing computational study has ever predicted if there is a thermodynamic limitation on the density of M-$N_4$ sites on the catalysts surface, how the different types (i.e., S1 and S2) of M-$N_4$ sites can be formed in a predictable way, and how the activity and stability of the M-$N_4$ sites should be modelled in a membrane electrode assembly (MEA) with a local ionomer environment.

In addition, the survey of literature reveals that the following aspects of computational electrocatalysis deserves further development. (1) The computational setup, procedure, and data format need be standardized in order to make the results from different research groups more readily comparable. It is particularly desirable that the uncertainties associated to the DFT methods, due to varied exchange-correlation functionals, K-point meshing, and choice of simulation cells,

could be systematically quantified. (2) Novel computational algorithm and methods are needed to treat the complexed electrochemical environment and integrate the catalyst activity with various transport processes in MEA, (3) Application of novel data informatics and machine learning methods to derive the relation between synthesis parameters, structures and density of active sites, and the performance (i.e., activity, selectivity, and durability) of the M-N-C catalysts for PEMFCs, (4) Future studies of M-N-C electrocatalyst stability are expected to further improve with both increased computational capabilities as well as more complete models of in situ thermokinetics, and (5) Improved understanding of how synthesis conditions lead to certain ORR active structures would aid in the application of electronic structure computational models to design real M-N-C catalyst systems.

**Acknowledgements**

The supports by the U.S. Department of Energy's (DOE) Fuel Cell Technology Office through the Electrocatalysis Consortium (ElectroCat) are acknowledged.

## References:


1. M. Lefèvre, E. Proietti, F. Jaouen and J.-P. Dodelet, *Science*, 2009, **324**, 71-74.
2. G. Wu, K. L. More, C. M. Johnston and P. Zelenay, *Science*, 2011, **332**, 443-447.
3. J. Li, M. Chen, D. A. Cullen, S. Hwang, M. Wang, B. Li, K. Liu, S. Karakalos, M. Lucero and H. Zhang, *Nature Catalysis*, 2018, **1**, 935-945.
4. M. Primbs, Y. Sun, A. Roy, D. Malko, A. Mehmood, M.-T. Sougrati, P.-Y. Blanchard, G. Granozzi, T. Kosmala and G. Daniel, *Energy & Environmental Science*, 2020, **13**, 2480-2500.
5. Y. He and G. Wu, *Accounts of Materials Research*, 2022, **3**, 224-236.
6. X. X. Wang, M. T. Swihart and G. Wu, *Nature Catalysis*, 2019, **2**, 578-589.
7. A. Mehmood, M. Gong, F. Jaouen, A. Roy, A. Zitolo, A. Khan, M.-T. Sougrati, M. Primbs, A. M. Bonastre and D. Fongalland, *Nature Catalysis*, 2022, **5**, 311-323.
8. H. Zhang, L. Osmieri, J. H. Park, H. T. Chung, D. A. Cullen, K. C. Neyerlin, D. J. Myers and P. Zelenay, *Nature Catalysis*, 2022, **5**, 455-462.
9. U. Martinez, S. Komini Babu, E. F. Holby, H. T. Chung, X. Yin and P. Zelenay, *Advanced Materials*, 2019, **31**, 1806545.
10. M. Shao, Q. Chang, J.-P. Dodelet and R. Chenitz, *Chemical Reviews*, 2016, **116**, 3594-3657.
11. H. He, Y. Lei, C. Xiao, D. Chu, R. Chen and G. Wang, *The Journal of Physical Chemistry C*, 2012, **116**, 16038-16046.
12. M. Zhu, C. Zhao, X. Liu, X. Wang, F. Zhou, J. Wang, Y. Hu, Y. Zhao, T. Yao and L.-M. Yang, *ACS Catalysis*, 2021, **11**, 3923-3929.
13. Z. Yang, X. Wang, M. Zhu, X. Leng, W. Chen, W. Wang, Q. Xu, L.-M. Yang and Y. Wu, *Nano Research*, 2021, **14**, 4512-4519.
14. C. Tang, L. Chen, H. Li, L. Li, Y. Jiao, Y. Zheng, H. Xu, K. Davey and S.-Z. Qiao, *Journal of the American Chemical Society*, 2021, **143**, 7819-7827.
15. A. Uddin, L. Dunsmore, H. Zhang, L. Hu, G. Wu and S. Litster, *ACS applied materials & interfaces*, 2019, **12**, 2216-2224.
16. S. Liu, C. Li, M. J. Zachman, Y. Zeng, H. Yu, B. Li, M. Wang, J. Braaten, J. Liu and H. M. Meyer, *Nature Energy*, 2022, **7**, 652-663.
17. L. Du, L. Xing, G. Zhang, M. Dubois and S. Sun, *Small Methods*, 2020, **4**, 2000016.
18. H. Zhang, H. Osgood, X. Xie, Y. Shao and G. Wu, *Nano Energy*, 2017, **31**, 331-350.
19. Y. He, S. Liu, C. Priest, Q. Shi and G. Wu, *Chemical Society Reviews*, 2020, **49**, 3484-3524.
20. D. Banham, S. Ye, K. Pei, J.-i. Ozaki, T. Kishimoto and Y. Imashiro, *Journal of Power Sources*, 2015, **285**, 334-348.
21. Y. Shao, J. P. Dodelet, G. Wu and P. Zelenay, *Advanced Materials*, 2019, **31**, 1807615.
22. Y. He, S. Hwang, D. A. Cullen, M. A. Uddin, L. Langhorst, B. Li, S. Karakalos, A. J. Kropf, E. C. Wegener and J. Sokolowski, *Energy & Environmental Science*, 2019, **12**, 250-260.
23. H. Zhang, H. T. Chung, D. A. Cullen, S. Wagner, U. I. Kramm, K. L. More, P. Zelenay and G. Wu, *Energy & Environmental Science*, 2019, **12**, 2548-2558.
24. J. K. Norskov, J. Rossmeisl, A. Logadottir, L. Lindqvist, J. R. Kitchin, T. Bligaard and H. Jonsson, *Journal of Physical Chemistry B*, 2004, **108**, 17886-17892.
25. A. Kulkarni, S. Siahrostami, A. Patel and J. K. Nørskov, *Chemical Reviews*, 2018, **118**, 2302-2312.
26. J. Greeley, I. E. L. Stephens, A. S. Bondarenko, T. P. Johansson, H. A. Hansen, T. F. Jaramillo, J. Rossmeisl, I. Chorkendorff and J. K. Nørskov, *Nature Chemistry*, 2009, **1**, 552-556.
27. J. A. Gauthier, C. F. Dickens, H. H. Heenen, S. Vijay, S. Ringe and K. Chan, *Journal of Chemical Theory and Computation*, 2019, **15**, 6895-6906.
28. H. H. Heenen, J. A. Gauthier, H. H. Kristoffersen, T. Ludwig and K. Chan, *The Journal of Chemical Physics*, 2020, **152**, 144703.

29. Q. Zhang and A. Asthagiri, *Catalysis Today*, 2019, **323**, 35-43.
30. T. Cheng, H. Xiao and W. A. Goddard, *The Journal of Physical Chemistry Letters*, 2015, **6**, 4767-4773.
31. M. Fishman, H. L. Zhuang, K. Mathew, W. Dirschka and R. G. Hennig, *Physical Review B*, 2013, **87**, 245402.
32. K. Mathew, R. Sundararaman, K. Letchworth-Weaver, T. A. Arias and R. G. Hennig, *The Journal of Chemical Physics*, 2014, **140**, 084106.
33. K. Mathew, V. C. Kolluru, S. Mula, S. N. Steinmann and R. G. Hennig, *The Journal of Chemical Physics*, 2019, **151**, 234101.
34. X. Zhao and Y. Liu, *Journal of the American Chemical Society*, 2020, **142**, 5773-5777.
35. Z. Duan and G. Henkelman, *ACS Catalysis*, 2019, **9**, 5567-5573.
36. J. S. Filhol and M. Neurock, *Angewandte Chemie International Edition*, 2006, **45**, 402-406.
37. R. Sundararaman, W. A. Goddard and T. A. Arias, *The Journal of Chemical Physics*, 2017, **146**, 114104.
38. J. Cheng and M. Sprik, *Physical Chemistry Chemical Physics*, 2012, **14**, 11245.
39. S. Trasatti, *Pure and Applied Chemistry*, 1986, **58**, 955-966.
40. R. Sundararaman and W. A. Goddard III, *The Journal of Chemical Physics*, 2015, **142**, 064107.
41. E. Skúlason, V. Tripkovic, M. E. Björketun, S. Gudmundsdottir, G. Karlberg, J. Rossmeisl, T. Bligaard, H. Jónsson and J. K. Nørskov, *The Journal of Physical Chemistry C*, 2010, **114**, 18182-18197.
42. K. Chan and J. K. Nørskov, *The Journal of Physical Chemistry Letters*, 2015, **6**, 2663-2668.
43. K. Chan and J. K. Nørskov, *The Journal of Physical Chemistry Letters*, 2016, **7**, 1686-1690.
44. J. D. Goodpaster, A. T. Bell and M. Head-Gordon, *The journal of physical chemistry letters*, 2016, **7**, 1471-1477.
45. Y. Guo, B. Li, S. Shen, L. Luo, G. Wang and J. Zhang, *ACS Applied Materials & Interfaces*, 2021, **13**, 16602-16610.
46. E. Sanville, S. D. Kenny, R. Smith and G. Henkelman, *Journal of Computational Chemistry*, 2007, **28**, 899-908.
47. M. Yu and D. R. Trinkle, *The Journal of Chemical Physics*, 2011, **134**, 064111.
48. J. K. Nørskov, F. Studt, F. Abild-Pedersen and T. Bligaard, *Fundamental Concepts in Heterogeneous Catalysis*, John Wiley & Sons, 2014.
49. A. Mehmood, M. Gong, F. Jaouen, A. Roy, A. Zitolo, A. Khan, M.-T. Sougrati, M. Primbs, A. M. Bonastre, D. Fongalland, G. Drazic, P. Strasser and A. Kucernak, *Nature Catalysis*, 2022, **5**, 311-323.
50. H. A. Hansen, V. Viswanathan and J. K. Nørskov, *The Journal of Physical Chemistry C*, 2014, **118**, 6706-6718.
51. A. M. Gómez-Marín and J. M. Feliu, *ChemSusChem*, 2013, **6**, 1091-1100.
52. M. Ferrandon, A. J. Kropf, D. J. Myers, K. Artyushkova, U. Kramm, P. Bogdanoff, G. Wu, C. M. Johnston and P. Zelenay, *The Journal of Physical Chemistry C*, 2012, **116**, 16001-16013.
53. G. Zhong, M. Xu, S. Xu, X. Fu, W. Liao and Y. Xu, *International Journal of Energy Research*, 2021, **45**, 10393-10408.
54. Y. Yang, K. Li, Y. Meng, Y. Wang and Z. Wu, *New Journal of Chemistry*, 2018, **42**, 6873-6879.
55. K. Liu, G. Wu and G. Wang, *The Journal of Physical Chemistry C*, 2017, **121**, 11319-11324.
56. J. Zhang, Z. Wang and Z. Zhu, *Journal of the Electrochemical Society*, 2015, **162**, F1262.
57. Y. Sha, T. H. Yu, B. V. Merinov, P. Shirvanian and W. A. Goddard, *The Journal of Physical Chemistry C*, 2012, **116**, 21334-21342.
58. M. Cherif, J.-P. Dodelet, G. Zhang, V. P. Glibin, S. Sun and F. Vidal, *Molecules*, 2021, **26**, 7370.

59. H. T. Chung, D. A. Cullen, D. Higgins, B. T. Sneed, E. F. Holby, K. L. More and P. Zelenay, *Science*, 2017, **357**, 479-484.
60. A. Zitolo, V. Goellner, V. Armel, M.-T. Sougrati, T. Mineva, L. Stievano, E. Fonda and F. Jaouen, *Nature Materials*, 2015, **14**, 937-942.
61. J. Li, S. Ghoshal, W. Liang, M.-T. Sougrati, F. Jaouen, B. Halevi, S. McKinney, G. McCool, C. Ma and X. Yuan, *Energy & Environmental Science*, 2016, **9**, 2418-2432.
62. X. Wan, X. Liu, Y. Li, R. Yu, L. Zheng, W. Yan, H. Wang, M. Xu and J. Shui, *Nature Catalysis*, 2019, **2**, 259-268.
63. J. Li, M. T. Sougrati, A. Zitolo, J. M. Ablett, I. C. Oğuz, T. Mineva, I. Matanovic, P. Atanassov, Y. Huang and I. Zenyuk, *Nature Catalysis*, 2021, **4**, 10-19.
64. A. Zitolo, N. Ranjbar-Sahraie, T. Mineva, J. Li, Q. Jia, S. Stamatin, G. F. Harrington, S. M. Lyth, P. Krtil and S. Mukerjee, *Nature Communications*, 2017, **8**, 1-11.
65. Z. Cai, P. Du, W. Liang, H. Zhang, P. Wu, C. Cai and Z. Yan, *Journal of Materials Chemistry A*, 2020, **8**, 15012-15022.
66. X. Sun, K. Li, C. Yin, Y. Wang, M. Jiao, F. He, X. Bai, H. Tang and Z. Wu, *Carbon*, 2016, **108**, 541-550.
67. R. Jasinski, *Nature*, 1964, **201**, 1212-1213.
68. Y. Jean, *Molecular orbitals of transition metal complexes*, OUP Oxford, 2005.
69. K. Liu, Y. Lei and G. Wang, *The Journal of chemical physics*, 2013, **139**, 204306.
70. Z. Duan and G. Wang, *Physical Chemistry Chemical Physics*, 2011, **13**, 20178.
71. J. Wang, Z. Huang, W. Liu, C. Chang, H. Tang, Z. Li, W. Chen, C. Jia, T. Yao, S. Wei, Y. Wu and Y. Li, *Journal of the American Chemical Society*, 2017, **139**, 17281-17284.
72. Z. Duan and G. Henkelman, *ACS Catalysis*, 2020, **10**, 12148-12155.
73. E. F. Holby and P. Zelenay, *Nano Energy*, 2016, **29**, 54-64.
74. S. Kattel and G. Wang, *The Journal of Physical Chemistry Letters*, 2014, **5**, 452-456.
75. G. Zhu, F. Liu, Y. Wang, Z. Wei and W. Wang, *Physical Chemistry Chemical Physics*, 2019, **21**, 12826-12836.
76. J. Zhang, Z. Wang and Z. Zhu, *Journal of Power Sources*, 2014, **255**, 65-69.
77. J. K. Nørskov, T. Bligaard, B. Hvolbæk, F. Abild-Pedersen, I. Chorkendorff and C. H. Christensen, *Chemical Society Reviews*, 2008, **37**, 2163.
78. K. S. Exner and H. Over, *Accounts of Chemical Research*, 2017, **50**, 1240-1247.
79. Y. Wang, Y.-J. Tang and K. Zhou, *Journal of the American Chemical Society*, 2019, **141**, 14115-14119.
80. U. Martinez, E. F. Holby, S. K. Babu, K. Artyushkova, L. Lin, S. Choudhury, G. M. Purdy and P. Zelenay, *Journal of the Electrochemical Society*, 2019, **166**, F3136-F3142.
81. J. Gao, H. B. Yang, X. Huang, S.-F. Hung, W. Cai, C. Jia, S. Miao, H. M. Chen, X. Yang, Y. Huang, T. Zhang and B. Liu, *Chem*, 2020, **6**, 658-674.
82. S. Wannakao, T. Maihom, K. Kongpatpanich, J. Limtrakul and V. Promarak, *Physical Chemistry Chemical Physics*, 2017, **19**, 29540-29548.
83. K. Liu, Y. Lei, R. Chen and G. Wang, in *Electrochemistry of N4 Macrocyclic Metal Complexes*, Springer, 2016, pp. 1-39.
84. Z. Shi and J. Zhang, *The Journal of Physical Chemistry C*, 2007, **111**, 7084-7090.
85. W. Zhong, Z. Wang, S. Han, L. Deng, J. Yu, Y. Lin, X. Long, M. Gu and S. Yang, *Cell Reports Physical Science*, 2020, **1**, 100115.
86. J. Yang, Z. Wang, C. X. Huang, Y. Zhang, Q. Zhang, C. Chen, J. Du, X. Zhou, Y. Zhang, H. Zhou, L. Wang, X. Zheng, L. Gu, L. M. Yang and Y. Wu, *Angewandte Chemie International Edition*, 2021, **60**, 22722-22728.

87. K. Liu, Z. Qiao, S. Hwang, Z. Liu, H. Zhang, D. Su, H. Xu, G. Wu and G. Wang, *Applied Catalysis B: Environmental*, 2019, **243**, 195-203.
88. Z. Duan and G. Henkelman, *Langmuir*, 2018, **34**, 15268-15275.
89. Y. Ping, R. J. Nielsen and W. A. Goddard III, *Journal of the American Chemical Society*, 2017, **139**, 149-155.
90. R. García-Cruz, E. Poulain, I. Hernández-Pérez, J. A. Reyes-Nava, J. C. González-Torres, A. Rubio-Ponce and O. Olvera-Neria, *The Journal of Physical Chemistry A*, 2017, **121**, 6079-6089.
91. Z. Duan and G. Henkelman, *ACS Catalysis*, 2020, **10**, 12148-12155.
92. J. P. Allen and G. W. Watson, *Physical Chemistry Chemical Physics*, 2014, **16**, 21016-21031.
93. T. Mineva, I. Matanovic, P. Atanassov, M.-T. Sougrati, L. Stievano, M. Clémancey, A. Kochem, J.-M. Latour and F. Jaouen, *ACS Catalysis*, 2019, **9**, 9359-9371.
94. T. He, Y. Chen, Q. Liu, B. Lu, X. Song, H. Liu, M. Liu, Y. N. Liu, Y. Zhang and X. Ouyang, *Angewandte Chemie International Edition*, 2022, **61**, e202201007.
95. F. Sun, F. Li and Q. Tang, *The Journal of Physical Chemistry C*, 2022, **126**, 13168-13181.
96. T. L. Cottrell, *The strengths of chemical bonds*, Butterworths Scientific Publications, 1958.
97. K. Liu, S. Kattel, V. Mao and G. Wang, *The Journal of Physical Chemistry C*, 2016, **120**, 1586-1596.
98. J. Gao, H. bin Yang, X. Huang, S.-F. Hung, W. Cai, C. Jia, S. Miao, H. M. Chen, X. Yang and Y. Huang, *Chem*, 2020, **6**, 658-674.
99. X. Xie, C. He, B. Li, Y. He, D. A. Cullen, E. C. Wegener, A. J. Kropf, U. Martinez, Y. Cheng and M. H. Engelhard, *Nature Catalysis*, 2020, **3**, 1044-1054.
100. E. Jung, H. Shin, B.-H. Lee, V. Efremov, S. Lee, H. S. Lee, J. Kim, W. Hooch Antink, S. Park and K.-S. Lee, *Nature Materials*, 2020, **19**, 436-442.
101. X. Zhao and Y. Liu, *Journal of the American Chemical Society*, 2021, **143**, 9423-9428.
102. S. Sun, N. Jiang and D. Xia, *The Journal of Physical Chemistry C*, 2011, **115**, 9511-9517.
103. J. Z. Li, H. G. Zhang, W. Samarakoon, W. T. Shan, D. A. Cullen, S. Karakalos, M. J. Chen, D. M. Gu, K. L. More, G. F. Wang, Z. X. Feng, Z. B. Wang and G. Wu, *Angewandte Chemie International Edition*, 2019, **58**, 18971-18980.
104. M. C. Elvington, H. T. Chung, L. Lin, X. Yin, P. Ganesan, P. Zelenay and H. R. Colón-Mercado, *Journal of the Electrochemical Society*, 2020, **167**, 134510.
105. V. K. Vashistha and A. Kumar, *Inorganic Chemistry Communications*, 2020, **112**, 107700.
106. R. Chen, H. Li, D. Chu and G. Wang, *The Journal of Physical Chemistry C*, 2009, **113**, 20689-20697.
107. S. Kattel and G. Wang, *The Journal of Physical Chemistry Letters*, 2014, **5**, 452-456.
108. U. Martinez, S. Komini Babu, E. F. Holby and P. Zelenay, *Current Opinion in Electrochemistry*, 2018, **9**, 224-232.
109. S. Kattel, P. Atanassov and B. Kiefer, *Physical Chemistry Chemical Physics*, 2014, **16**, 13800-13806.
110. S. Kattel, P. Atanassov and B. Kiefer, *Physical Chemistry Chemical Physics*, 2013, **15**, 148-153.
111. S. Kattel, P. Atanassov and B. Kiefer, *The Journal of Physical Chemistry C*, 2012, **116**, 8161-8166.
112. E. F. Holby and C. D. Taylor, *Applied Physics Letters*, 2012, **101**, 064102.
113. E. F. Holby, G. Wu, P. Zelenay and C. D. Taylor, *ECS Transactions*, 2013, **50**, 1839-1845.
114. E. F. Holby, G. Wu, P. Zelenay and C. D. Taylor, *The Journal of Physical Chemistry C*, 2014, **118**, 14388-14393.
115. E. F. Holby and C. D. Taylor, *Scientific Reports*, 2015, **5**, 9286.
116. V. P. Glibin and J.-P. Dodelet, *Journal of the Electrochemical Society*, 2017, **164**, F948-F957.
117. E. F. Holby, G. Wang and P. Zelenay, *ACS Catalysis*, 2020, **10**, 14527-14539.
118. T. Patniboon and H. A. Hansen, *ACS Catalysis*, 2021, **11**, 13102-13118.
119. M. Chen, X. Li, F. Yang, B. Li, T. Stracensky, S. Karakalos, S. Mukerjee, Q. Jia, D. Su, G. Wang, G. Wu and H. Xu, *ACS Catalysis*, 2020, **10**, 10523-10534.

120. N. Yang, L. Peng, L. Li, J. Li, Q. Liao, M. Shao and Z. Wei, *Chemical Science*, 2021, **12**, 12476-12484.
121. E. F. Holby, *Fuel Cells*, 2016, **16**, 669-674.
122. K. L. Svane, M. Reda, T. Vegge and H. A. Hansen, *ChemSusChem*, 2019, **12**, 5133-5141.